Acta Cryst B
STRUCTURAL SCIENCE
CRYSTAL ENGINEERING
MATERIALS
ISSN 2052-5206

Room-temperature synthesis of a new stable $(N_2H_4)WO_3$ compound: a route for hydrazine trapping

F. Giovannelli,[a]* C. Mathieu,[a] K. Fritsch,[b] K. Adil,[c,d] F. Goutenoire,[d] K. Habicht[b] and F. Delorme[a]

[a]Université François Rabelais de Tours, CNRS, INSA CVL, GREMAN UMR 7347, IUT de Blois, 15 rue de la chocolaterie, CS 2903, Blois, Cedex 41150, France, [b]Helmholtz-Zentrum Berlin für Materialien und Energie GmbH, Berlin 14109, Germany, [c]KAUST (King Abdullah University of Science and Technology), Thuwal, Saudi Arabia, and [d]IMMM (Institute of Materials and Molecules of Mans), UMR-CNRS 6283, Le Mans University, 72085 Le Mans, Cedex 9, France.
*Correspondence e-mail: fabien.giovannelli@univ-tours.fr

Received 18 September 2018
Accepted 3 January 2019

Edited by P. Bordet, Institut Néel, France

Keywords: hybrid compound; tungsten oxide; hydrazine trapping.

CCDC reference: 1846977

Supporting information: this article has supporting information at journals.iucr.org/b

A new $(N_2H_4)WO_3$ compound has been obtained by mixing WO_3 and aqueous hydrazine solution at room temperature for 24 h. The reaction is catalyzed by the presence of lithium. X-ray, synchrotron and neutron diffraction techniques have shown that the material crystallizes in trigonal space group $P3_221$ (No. 154). Chains of distorted WO_4 tetrahedra extend along the *a* axis of the unit cell, linked by a corner-sharing oxygen atom: the N_2H_4 are in the voids between them. The thermal characterization shows that this new compound is stable up to 220°C, greatly beyond the boiling point of N_2H_4 (114°C); thus making it a promising candidate for catalysis or trapping applications.

1. Introduction

Hydrazine, N_2H_4, is a well known compound used as a precursor for several pesticide and pharmaceutical agents (Lukin *et al.*, 2006; Amarnath *et al.*, 1991; Wasserman & Vinick, 1973; Bashore *et al.*, 2003). It is characterized by a high energy density, which makes it suitable for use as a propellant for rockets and satellites or as fuel in fuel cells (Gu *et al.*, 2008; Yin *et al.*, 2008). Moreover, hydrazine is also often used in chemistry due to its reducing power, where it can be used as an antioxidant or corrosion inhibitor (Arkhipov *et al.*, 1997). For instance, in thermal and nuclear plants, hydrazine is added to the coolant water in order to remove dissolved oxygen, hence preventing corrosion (Arkhipov *et al.*, 1997). However, hydrazine is a highly reactive and toxic chemical considered a neurotoxin and carcinogen (Moloney & Prough, 1983; Garrod *et al.*, 2005). Direct exposure to hydrazine may cause harmful health effects for humans. Thus, many studies have focused on hydrazine sensors based on different kinds of classical measurement techniques such as chromatography, fluorimetry, spectrophotometry and electrochemistry (Nagaokaa *et al.*, 2006; Gojon *et al.*, 1999; Davidson, 1982; Ensafi & Rezaei, 1998; Song *et al.*, 2001; Zare & Habibirad, 2006). Among them, different amperometric hydrazine sensors based on oxide electrodes have been investigated. Different oxides such as ZnO, CuO, $CoFe_2O_4$, Co_3O_4, WO_3 and Mn_2O_3 have been tested as electrode materials (Umar *et al.*, 2009; Liu *et al.*, 2015; Wang *et al.*, 2009; Ding *et al.*, 2011; Zhou *et al.*, 2016; Oh *et al.*, 2015; Shukla *et al.*, 2014). Such sensors are efficient in detecting traces of hydrazine with high sensitivity and a low detection limit. In the case of large hydrazine pollution, two

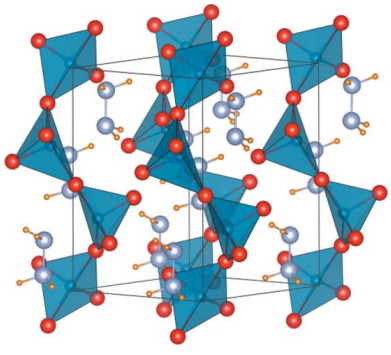

strategies can be developed: the first consists of consuming hydrazine in a reaction that leads to non-hazardous compounds. In the presence of large amounts of hydrazine, some oxides could oxidize hydrazine due to its high reducing power. Clark & Pickering (1967) have shown that silver oxide could be reduced to silver metal by hydrazine. In some cases, however, exposure to hydrazine does not lead to metals but to reduced oxides. For example, Giovannelli *et al.* (2009) demonstrated that a powder of birnessite ($K_xMnO_2{\cdot}yH_2O$) treated in an aqueous solution with hydrazine results in the formation of Mn_3O_4 nanoparticles. Another more environmentally friendly approach is to trap the hydrazine molecule in a solid framework, producing a hybrid material, comparable to cations in clays or anions in layered double hydroxides (Matthes, 1999; Delorme *et al.*, 2007). Moreover, for many years, hybrid materials have also attracted the attention of many research groups as an opportunity to take advantage the properties of the constituents or to generate new material properties (Sanchez *et al.*, 2005). Among them, the most successful examples are organoclays (Bottero *et al.*, 1994), dye-sensitized solar cells (O'Regan & Gratzel, 1991) and metal–organic frameworks (Férey, 2005).

Tungsten oxide, WO_3, appears to be a good candidate for the formation of a hybrid material with hydrazine. Indeed, from WO_3, which exhibits a ReO_3 structure, many different structures can be obtained. With a slight degree of reduction, crystallographic shear planes could appear to accommodate the lack of oxygen and lead to the formation of different phases (Tilley, 1995). For a higher degree of reduction, the octahedral coordination of W leads, in part, to pentagonal bipyramidal coordination and the creation of channels in the structure. Generally, these phases can also be stabilized by the addition of cations in the channels to form M_xWO_3 ($M = Na^+$, Li^+, K^+, NH_4^+, *etc.*), the well known bronze structure (Tilley, 1995; Dickens & Whittingham, 1968).

Hydrazine is also thought to reduce WO_3, leading to the creation of channels in the structure and allowing the insertion of molecules inside the structure. In this paper, we demonstrate a route for the synthesis of a new stable hybrid crystal structure in order to trap hydrazine.

2. Materials and methods

Lithium hydroxide (LiOH 99.99%), lithium acetate, ($C_2H_3LiO_2$ 99.99%), WO_3 (99%) and hydrazine monohydrate $N_2H_4{\cdot}H_2O$ (98%) were purchased from Sigma–Aldrich. Liquid HNO_3 (65%) was purchased from Fluka. All reactants were used without further purification. An aqueous solution of lithium nitrate (0.5 mol l^{-1}) was obtained by mixing lithium hydroxide and HNO_3.

We performed three different experiments to study the possible N_2H_4 trapping in WO_3. For the first experiment, 10 g of WO_3 and 15.65 g of hydrazine were mixed under stirring and air at room temperature for 24 h. The slurry was centrifuged for 10 min at 4000 r.p.m. (Thermo Sorvall ST 16 centrifuge). The supernatant was eliminated and the sample was washed three times with room-temperature deionized water. The sample was subsequently dried in a furnace at 60°C for 24 h.

For the second experiment, an aqueous solution of lithium nitrate (6.3 ml, 0.5 mol l^{-1}) was added to WO_3 before the addition of hydrazine. Finally, when lithium acetate was used as a precursor, lithium acetate aqueous solution (50 ml, 0.063 mol l^{-1}) was added. Regardless of which lithium salt chosen, the molar ratio of Li/W was kept constant and equal to 0.07. For the latter two approaches, centrifuging and drying proceeded after the addition of hydrazine in the same manner as with the first experiment.

Powder X-ray diffraction (PXRD) patterns have been collected at room temperature on a Bruker D8 Advance $\theta/2\theta$ diffractometer equipped with a Linxeye energy-dispersive one-dimensional detector, using Cu $K\alpha$ radiation and operating at 40 kV and 40 mA. The scans have been recorded from 10 to 80°(2θ) with a step of 0.02° and a counting time of 0.5 seconds per step.

High-temperature X-ray diffraction patterns were collected on a Bragg–Brentano diffractometer (MPD-PRO Panalytical) equipped with a linear detector X'Cellerator and an Anton Paar HTK12 furnace. The high-temperature X-ray diffraction patterns were collected overnight in the 2θ range 5–65° over a temperature range from 40 to 440°C in 40°C steps.

High-quality powder neutron diffraction data were obtained at room temperature and at 100 K using the time-of-flight instrument POWGEN at the Spallation Neutron Source (SNS) at Oak Ridge National Laboratory, Oak Ridge, USA (Huq *et al.*, 2011), with a 1 Å-wavelength band centered at λ = 1.333 Å. For these measurements, a sample of ∼4 g was loaded in a standard vanadium can. High-resolution synchrotron powder diffraction data were collected at the same temperatures on beamline 11-BM at the Advanced Photon Source at Argonne National Laboratory, USA (Wang *et al.*, 2008), using an average wavelength of 0.413341 Å. Discrete detectors covering an angular range from −6 to 16° in 2θ were scanned over a 34° 2θ range, with data points collected every 0.001° in 2θ and at a scan speed of 0.01° s^{-1}. Both neutron and synchrotron data sets were analyzed with the *FullProf* (Rodriguez-Carvajal, 1993) program suite.

The microstructures of the samples were observed using a Quanta200 (FEI) scanning electron microscope (SEM) coupled with an Oxford Inca energy-dispersive X-ray (EDX) spectrometer. Elemental analyses (for N, W and Li) were performed at the Service Central d'Analyses (CNRS, Vernaison, France). Thermogravimetric analyses (TGA) have been recorded on a TGA-A7 (Perkin–Elmer) analyzer using flowing synthetic air (25 ml min^{-1}) at a heating rate of 10°C min^{-1} up to 800°C.

In order to reveal the presence of ammonia (NH_3) or ammonium cations (NH_4^+) in the samples, Nessler reagent [0.09 mol l^{-1} solution of potassium tetraiodomercurate(II) ($K_2[HgI_4]$) in 2.5 mol l^{-1} potassium hydroxide] was employed (Vogel & Svehla, 1979). For this purpose, the powder (16 mg) was dissolved in NaOH solution (5 ml, 2*M*). Finally, five droplets of the Nessler reagent were added. Nessler reagent reacts with NH_3. Depending on the concentration of NH_3, the

Nessler reagent yields various concentrations of Millon's base molecules, thus generating colours ranging from orange to brown.

3. Results and discussion

The first experimental route consists of the addition of aqueous hydrazine to WO_3 powder and stirring the mixture for 24 h. The corresponding room-temperature XRD pattern is shown in Fig. 1 and compared with that of the WO_3 precursor. The latter pattern exhibits a monoclinic symmetry (PDF card 00-043-1035), which corresponds to the stable phase at room temperature of non-intercalated WO_3. From the appearance of new reflections in the XRD pattern (indicated by arrows) for aqueous hydrazine + WO_3, we conclude that a reaction between the two compounds occurs. However, the main phase is still WO_3 and it is difficult to attribute these new peaks to a known phase. This reaction could be related to the insertion of hydrazine in the channel of the WO_3 structure, as already shown in the bronze structure (Dickens & Whittingham, 1968).

Thus, in the case of the insertion hypothesis, the addition of lithium salt could increase the yield of the reaction as Li^+ insertion into Li_xWO_3 was easily achieved in previous work (Tilley, 1995; Dickens & Whittingham, 1968).

Therefore, in the second experiment, WO_3 was first mixed with an aqueous solution of lithium nitrate before adding hydrazine to the solution. This mixture was then stirred again at room temperature for 24 h. After drying, this reaction led to a pale-blue powder. The corresponding room-temperature XRD pattern is shown in Fig. 2 and is clearly different from that of the WO_3 phase. It does not correspond to any of the other precursors (lithium nitrate or N_2H_4). Moreover, it cannot be identified with any of the available JCPDS cards.

In order to assess the influence of the precursors on the reaction product, a number of different syntheses with slight variations were performed. First, in order to evaluate the role of the Li^+ counterion, a similar synthesis was carried using lithium acetate instead of the lithium nitrate salt. A pale-blue powder is also obtained. The XRD pattern is similar to the one obtained with lithium nitrate; however, a small amount of the

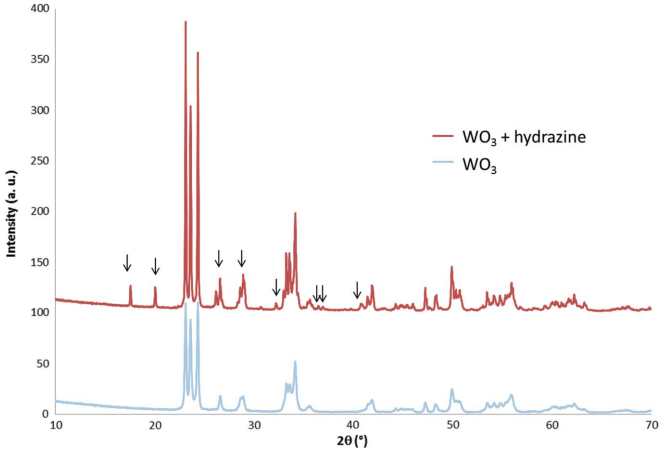

Figure 1
XRD patterns of aqueous $N_2H_4 + WO_3$ (after mixing for 24 h) and the precursor WO_3.

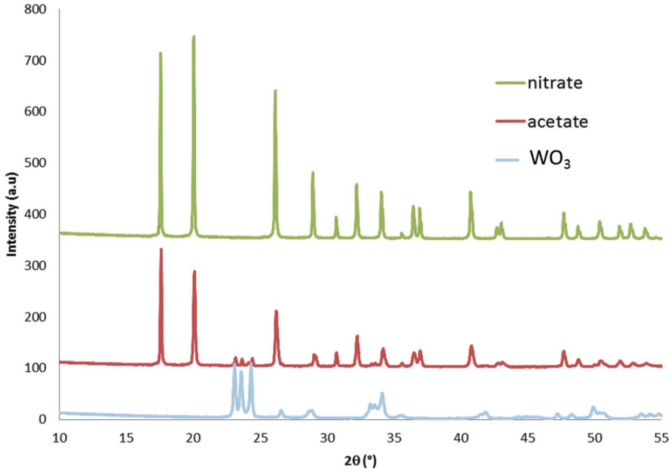

Figure 2
XRD patterns of WO_3 (bottom), WO_3 with hydrazine and lithium acetate (middle), and WO_3 with hydrazine and lithium nitrate (top).

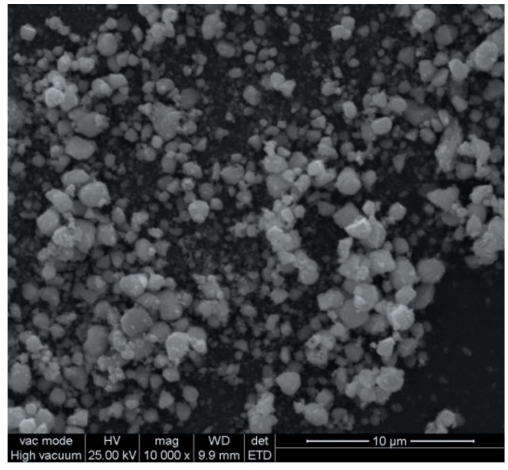

(*a*)

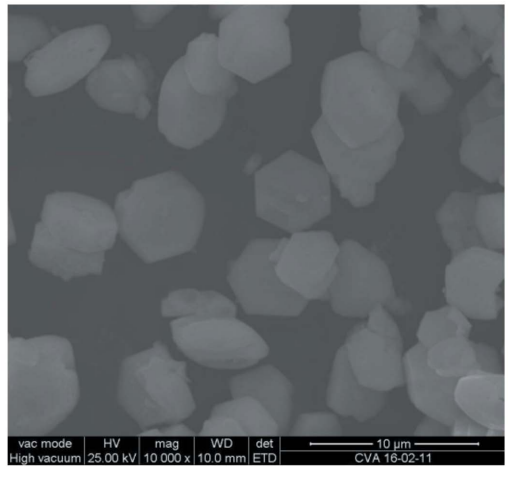

(*b*)

Figure 3
SEM images of WO_3 (*a*) and the pale-blue powder obtained with the lithium nitrate precursor (*b*).

WO_3 precursor appears to remain in the sample. Therefore, the counterion does not appear to play any prominent role in the synthesis of the phase, whereas the reaction is not totally complete when using the lithium acetate salt.

SEM images show WO_3 particles to be micrometre-sized [Fig. 3(*a*)], whereas the pale-blue powder exhibits particles which are hexagonal platelets and several micrometres across [Fig. 3(*b*)]. The different morphology between the two powders means that the reaction leading to the pale-blue powder is not a topotactic reaction. Therefore, the reaction is not the result of a simple insertion of hydrazine into the channels of the WO_3 bronze structure, but is a dissolution and recrystallization phenomenon.

The EDS analysis of the resulting blue powder indicates the presence of nitrogen in addition to tungsten and oxygen. These nitrogen atoms come from either hydrazine or the nitrate anions of the $LiNO_3$ solution. In order to determine the origin of such nitrogen atoms, EDS analysis has been performed on the pale-blue powder obtained with the lithium acetate salt: it still reveals the presence of nitrogen atoms, showing that the latter come from hydrazine. As EDS analysis is not efficient for quantitative analysis of light elements such as nitrogen or lithium, elemental analysis has been performed on the compound synthesized with the lithium nitrate salt (N 11.17 wt%, W 66.01 wt%). The atomic ratio N/W is close to 2.2 and the lithium content is very low (10 p.p.m.). Therefore, lithium acts as a catalyst for the reaction.

Fig. 4 shows the thermal decomposition behaviour of the pale-blue powder sample. Three weight losses of 2.3, 11.1 and 1.3% are observed at 110, 250 and 360°C, respectively.

Fig. 5 shows the evolution of the XRD pattern of the pale-blue powder with temperature. The structure is stable up to 200°C. Between 200 and 240°C, a structural transition gradually takes place which is consistent with the second weight loss. The resulting powder is stable up to 280°C. The main peaks of the resulting powder XRD pattern (2θ values of 14, 24, 28, 36, 48 and 56°) could be matched to a hexagonal $(NH_4)_xWO_3$ phase (Reis *et al.*, 1992; Huo *et al.*, 2004; Szilágyi *et al.*, 2008) (Fig. 6). However, the XRD pattern also exhibits a broad peak from 20 to 35° which could correspond to an amorphous phase. Moreover, the three most intense peaks of WO_3 are also present with a low intensity and some small peaks are not identified (2θ values of 18, 23, 28, 30 and 46°). So, between 240 and 280°C, the resulting powder is composed of several phases. When the temperature increases, a second structural transition occurs at 300°C and the XRD pattern indicates a transition to WO_3 (and a loss of NH_4^+). This could be related to the third weight loss (360°C) as TGA measurements are dynamic whereas XRD measurements are performed at specific temperatures step-by-step after a stabilization period of several minutes.

Due to the possible occurrence of NH_4^+ cations in the compound, the Nessler test (Vogel & Svehla, 1979) was carried out on the as-grown pale-blue powder. In the presence of NH_4^+, the Nessler test leads to a brown colour. However, in the case of the pale-blue powder, the obtained solution is grey, indicating the lack of NH_4^+ cations.

In view of interpreting this grey colour, the Nessler test was also performed on the hydrazine N_2H_4 solution, and a similar grey colour was obtained. The grey colour could thus be linked to the occurrence of the complexation of iodine by hydrazine. Thermal treatments have been performed on the pale-blue powder for 6 h under air at 120 and 320°C and the Nessler test was carried out on each resulting powder. At

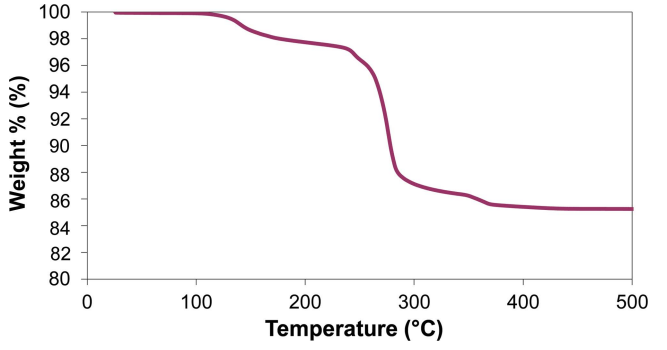

Figure 4
TGA of the pale-blue powder obtained with the lithium nitrate precursor.

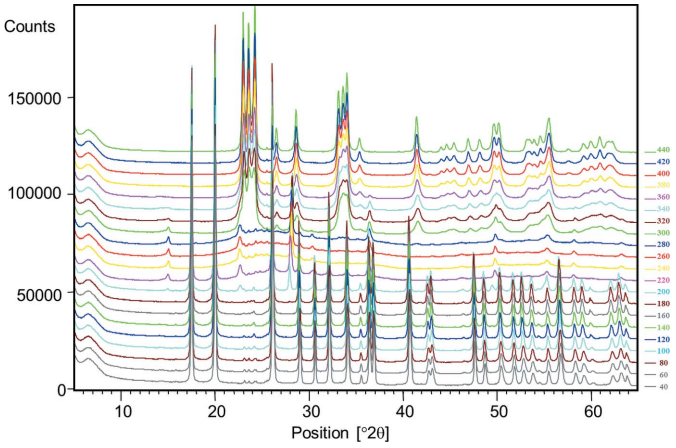

Figure 5
XRD patterns of the pale blue powder obtained with the lithium nitrate precursor *versus* temperature.

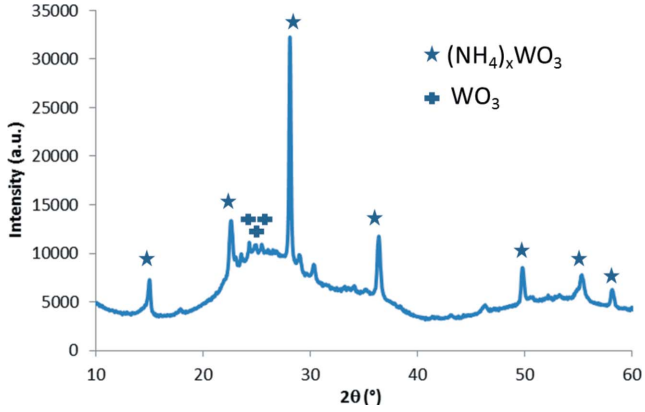

Figure 6
XRD pattern of pale-blue powder obtained with the lithium nitrate precursor heated at 240°C.

120°C, the solution is grey, confirming the presence of hydrazine. A brown colour appears at 320°C, which is characteristic of presence of NH_4^+ in solution. This means that at this temperature, the hydrazine has decomposed into NH_4^+. This is consistent with the presence of the observed $(NH_4)_xWO_3$ phase matched to the most intense reflections in the XRD pattern (Fig. 5).

To summarize, the first weight loss at 110°C is due to water evaporation; the second weight loss at 250°C is then linked to the decomposition of N_2H_4 into NH_4^+, leading to an intermediate phase. The third weight loss at 360°C can be attributed to the decomposition of $(NH_4)_xWO_3$, leading to WO_3. Hence, the weight loss between 150 and 400°C allows evaluation of the N_2H_4 content in the pale-blue powder. The atomic ratio N/W calculated from the TGA is 2.1, which is consistent with the ratio calculated by the elemental analysis (N 11.17 wt%, W 66.01 wt%). Hence, the chemical formula of the pale-blue powder could be $(N_2H_4)WO_3$.

The structure determination was performed *ab initio* from the room-temperature X-ray powder diffraction data. The cell parameters were obtained from auto-indexed programs *Treor* (Werner *et al.*, 1985), *Dicvol* (Boultif & Louër, 2004) and *McMaille* (Le Bail, 2004) implemented in *HighScorePlus* (Degen *et al.*, 2014), leading to a hexagonal cell with $a \simeq 5.82$ Å and $c \simeq 9.21$ Å and a figure of merit of 68. Fine analysis of the systematic extinction leads to the reflection condition on 00l of $l = 3n$. This last condition gives the possible trigonal space groups $P3_1$-- and $P6_2$--. The determination of the partial structure was primarily conducted with the XRD pattern using the intensities of the first 79 Bragg peaks extracted by the Le Bail procedure in the space group $P3_221$. The real-space Monte Carlo method implemented in *Espoir* (Le Bail, 2001) was used. A partial structure solution was found composed of one 3*a* tungsten position and two 3*b* and 6*c* oxygen positions. This partial structure forms interconnected WO_4 tetrahedra leading to the final composition of WO_3. The previous Rietveld refinement of the partial structure gives a good reliability factor $R_{Bragg} \simeq 0.045$. The reaction of N_2H_4 with WO_3 leads to a distinct change in coordination around the W atom. The W tetrahedral coordination is not the most common coordination but exists in different structures (see, for example, Mary *et al.*, 1996; Chambrier *et al.*, 2014). The resulting chains of corner-sharing WO_4 tetrahedra are similar to the crystal structure of the lighter homologue of WO_3, chromium(VI) oxide (CrO_3) (Stephens & Cruickshank, 1970).

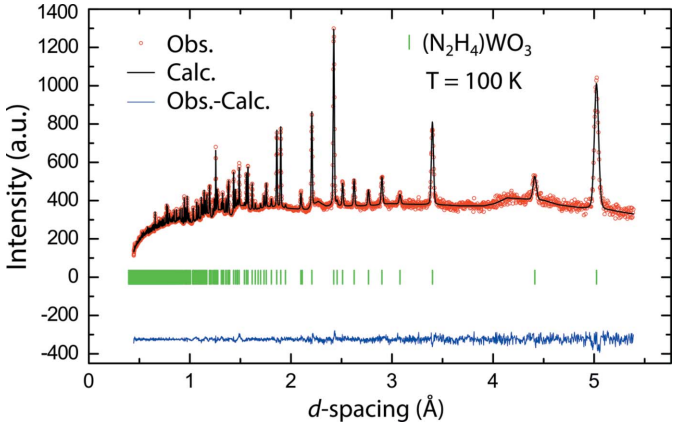

Figure 7
Rietveld refinement of $(N_2H_4)WO_3$ at $T = 100$ K of neutron powder data collected at POWGEN, SNS. Reliability factors: $R_{wp} = 0.131$, $R_f = 0.0776$, $\chi^2 = 3.95$.

Table 1
Structural parameters for $(N_2H_4)WO_3$ at 100 K.

Space group $P3_221$ (No. 154); $a = b = 5.7984$ (1) Å, $c = 9.2341$ (3) Å, $\alpha = \beta = 90°$, $\gamma = 120°$. Wyckoff positions: W in 3*a*, O1 in 3*b*, O2, N6, H1 and H2 in 6*c*. The site occupancies were not refined. Each site is assumed to be fully occupied.

Atom	x	y	z	U_{iso} (Å^2)
W	0	0.1921 (5)	$\frac{1}{3}$	0.002
O1	0.2351 (5)	0.1949 (5)	$\frac{1}{2}$	0.010 (7)
O2	0.2351 (5)	0.4920 (6)	0.2537 (2)	0.0054 (4)
N	0.7493 (2)	0.7427 (1)	0.579 (1)	0.0066 (3)
H1	0.6138 (8)	0.795 (1)	0.6124 (6)	0.026 (1)
H2	0.674 (1)	0.5512 (4)	0.6140 (6)	0.026 (1)

Table 2
Bond distances (Å) and bond angles (°) for $(N_2H_4)WO_3$ at 100 K.

N—H	1.022 (6)	W—O1	1.905 (2)	∠N—N—H1	115.6 (3)
N—N	1.460 (2)	W—O2	1.747 (3)	∠N—N—H2	110.1 (4)
				∠W—O1—W	145.0 (1)

The full crystal structure was then determined by Rietveld refinement from both synchrotron and neutron diffraction data sets measured at 100 K, making use of the complementary nature of X-rays and neutrons as probes with different scattering properties and contrasts (form factors), which is especially important here in order to identify the atomic positions of the hydrogen atoms (using neutron diffraction). The space group, lattice parameters and atomic positions of the heavy tungsten, the oxygen as well as the nitrogen atoms were first determined from the synchrotron data and used as initial parameters for the refinement of the neutron data. In particular, the locations of the hydrogen atoms in the structure were determined by keeping their atomic displacement parameters (ADPs) fixed and constraining their distance to be less than 1.1 Å from the nitrogen atom, at and above which, their bonding would become unphysical. In a next step, after the atomic positions of the H atoms were determined, their ADPs were refined under the assumption that both hydrogen atoms behave similarly at 100 K. Alternative scenarios including different ADPs for the two hydrogen sites or non-isotropic hydrogen ADPs have also been tested but have resulted in lower refinement quality. The refinement results are shown in Fig. 7, the corresponding structural parameters are given in Table 1 and the geometrical parameters are given in Table 2.

The Rietveld refinement indicates that the material crystallizes in the trigonal space group $P3_221$ (No. 154) [this space group is consistent with the hexagonal shape of the crystallites of pale-blue powder, as observed by SEM; see Fig. 3(*b*)]. The crystal structure of $(N_2H_4)WO_3$ can be derived from the monoclinic WO_3 structure. There, chains of distorted WO_4 tetrahedra extend along the *a* axis of the unit cell, linked by a

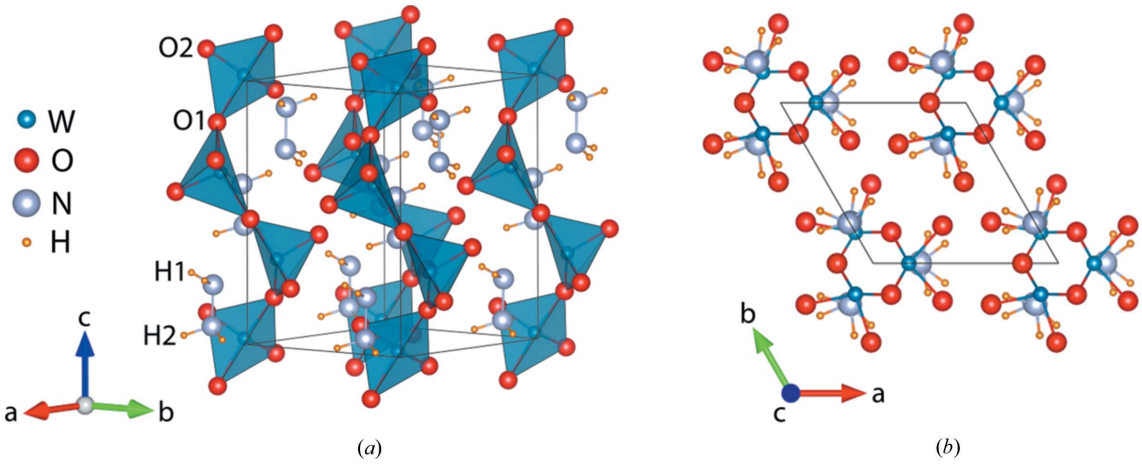

Figure 8
Crystal structure of $(N_2H_4)WO_3$ at 100 K. (*a*) Side view showing the distorted zigzag chains of WO_4 tetrahedra and the position of the N_2H_4 molecules in the structure. (*b*) Top view showing the symmetry and connectivities of the WO_4 chains as well as the asymmetric eclipsed orientation of the N_2H_4 molecules.

corner-sharing oxygen atom and forming a W—O—W angle of 153.4 (3)° (see Fig. 8). Upon incorporation of N_2H_4, the monoclinic WO_3 unit-cell transforms into a trigonal cell with lattice parameters $a = b = 5.79842\ (12)$ Å and $c = 9.23411\ (3)$ Å, in which the distorted WO_4 tetrahedra form chains along the *c* axis of the unit cell with a somewhat narrower W—O—W angle of 145.0 (1)°. This narrower angle can be associated with a larger tilting of the respective WO_4 tetrahedra, which incorporate the N_2H_4 molecules in the voids between them. These N_2H_4 molecules are found to have a similar structure to that of free N_2H_4 molecules (Yamaguchi *et al.*, 1959; Kohata *et al.*, 1982; Feller *et al.*, 2017). The N—N distance is determined to be 1.460 (2) Å [compared with 1.453 (5) Å obtained from far infrared spectra (Yamaguchi *et al.*, 1959)] and the N—H distances are found to be 1.022 (6) Å, which are in excellent agreement with earlier studies (Yamaguchi *et al.*, 1959; Kohata *et al.*, 1982; Feller *et al.*, 2017). Interestingly, in contrast to the free molecules for which the N—N—H angles were reported as ∼112–112.5° in previous work, assuming a symmetric form of N_2H_4, we find two different angles N—N—H1 = 115.6 (3)° and N—N—H2 = 110.1 (4)°, indicating a slight distortion of the N_2H_4 molecule in the surrounding WO_4 tetrahedral environment of the crystal structure. It can be intuitively understood by the presence of the nitrogen lone pairs and the corresponding arrangement of the hydrogen atoms to minimize electrostatic interactions, leading to an eclipsed conformation in which the two H—N—H parts of the molecule are rotated with respect to each other. Similar angles have been reported by a recent computational study (Feller *et al.*, 2017).

4. Conclusions

A new compound has been obtained by contacting WO_3 and aqueous hydrazine solution at room temperature for a duration of 24 h. It results from the self-assembly of ionic species in solution. The reaction is catalyzed by the presence of lithium. N_2H_4 molecules remain encapsulated within the negatively charged poly-tungstate cage where they interact with WO_3 tetrahedra. This new phase is able to trap hydrazine in a solid phase and could be a way to control hydrazine pollution. Indeed, instead of generating a metal or oxide nanoparticles that could represent a hazard for the environment as conventional hydrazine treatment methods do, N_2H_4 is trapped in large micrometre-sized particles. Moreover, this compound is stable up to 220°C and WO_3 can be restored by a treatment at 330°C. Finally, as the boiling point of N_2H_4 is 114°C, this structure retains N_2H_4 molecules at higher temperatures in a solid form which could lead to interesting catalytic reactions. The next steps will be to study intercalation and deintercalation in this structure (kinetics, competition, other N-bearing compounds, *etc.*).

Funding information

We acknowledge the use of the POWGEN instrument at the Spallation Neutron Source, a US Department of Energy, Office of Science User Facility operated by Oak Ridge National Laboratory. The use of beamline BM-11 at the Advanced Photon Source at Argonne National Laboratory is supported by the US Department of Energy, Office of Science, Office of Basic Energy Sciences (contract No. DE-AC02-06CH11357).

References

Amarnath, V., Anthony, D. C., Amarnath, K., Valentine, W. M., Wetterau, L. A. & Graham, D. G. (1991). *J. Org. Chem.* **56**, 6924–6931.
Arkhipov, O. P., Bugaenko, V. L., Kabakchi, S. A. & Pashevich, V. I. (1997). *At. Energy*, **82**, 92–98.
Bashore, C. G., Samardjiev, I. J., Bordner, J. & Coe, J. W. (2003). *J. Am. Chem. Soc.* **125**, 3268–3272.
Bottero, J. Y., Khatib, K., Thomas, F., Jucker, K., Bersillon, J. L. & Mallevialle, J. (1994). *Water Res.* **28**, 483–490.
Boultif, A. & Louër, D. (2004). *J. Appl. Cryst.* **37**, 724–731.

Chambrier, M. H., Le Bail, A., Giovannelli, F., Redjaïmia, A., Florian, P., Massiot, D., Suard, E. & Goutenoire, F. (2014). *Inorg. Chem.* **53**, 147–159.
Clark, A. J. & Pickering, W. F. (1967). *J. Inorg. Nucl. Chem.* **29**, 836–838.
Davidson, A. G. (1982). *Analyst*, **107**, 422–427.
Degen, T., Sadki, M., Bron, E., König, U. & Nénert, G. (2014). *Powder Diffr.* **29**, S13–S18.
Delorme, F., Seron, A., Gautier, A. & Crouzet, C. (2007). *J. Mater. Sci.* **42**, 5799–5804.
Dickens, P. G. & Whittingham, M. D. (1968). *Q. Rev. Chem. Soc.* **22**, 30–44.
Ding, Y., Hou, C., Li, B. & Lei, Y. (2011). *Electroanalysis*, **23**, 1245–1251.
Ensafi, A. A. & Rezaei, B. (1998). *Talanta*, **47**, 645–649.
Feller, D., Bross, D. H. & Ruscic, B. (2017). *J. Phys. Chem. A*, **121**, 6187–6198.
Férey, G. (2005). *Nature*, **436**, 187–188.
Garrod, S., Bollard, M. E., Nicholls, A. W., Connor, S. C., Connelly, J., Nicholson, J. K. & Holmes, E. (2005). *Chem. Res. Toxicol.* **18**, 115–122.
Giovannelli, F., Chartier, T., Autret-Lambert, C., Delorme, F., Zaghrioui, M. & Seron, A. (2009). *J. Solid State Chem.* **182**, 1021–1026.
Gojon, C., Duréault, B., Hovnanian, N. & Guizard, C. (1999). *J. Sol.-Gel Sci. Technol.* **14**, 163–173.
Gu, H., Ran, R., Zhou, W., Shao, Z., Jin, W., Xu, N. & Ahn, J. (2008). *J. Power Sources*, **177**, 323–329.
Huo, L., Zhao, H., Mauvy, F., Fourcade, S., Labrugere, C., Pouchard, M. & Grenier, J. (2004). *Solid State Sci.* **6**, 679–688.
Huq, A., Hodges, J. P., Gourdon, O. & Heroux, L. (2011). *Z. Kristallogr.* **1**, 127–135.
Kohata, K., Fukuyama, T. & Kuchitsu, K. (1982). *J. Phys. Chem.* **86**, 606–606.
Le Bail, A. (2001). *Mater. Sci. Forum*, **378–381**, 65–70.
Le Bail, A. (2004). *Powder Diffr.* **19**, 249–254.
Liu, J., Shen, J., Li, M. & Guo, L. (2015). *Chin. Chem. Lett.* **26**, 1478–1484.
Lukin, K., Hsu, M. C., Fernando, D. & Leanna, M. R. (2006). *J. Org. Chem.* **71**, 8166–8172.
Mary, T. A., Evans, J. S. O., Vogt, T. & Sleight, A. W. (1996). *Science*, **272**, 90–92.
Matthes, W. (1999). *Clays Clay Miner.* **47**, 617–629.
Moloney, S. J. & Prough, R. A. (1983). *Rev. Biochem. Toxicol.* **5**, 313–346.
Nagaokaa, M. H., Nagaoka, H., Kondo, K., Akiyama, H. & Maitani, T. (2006). *Chem. Pharm. Bull.* **54**, 922–924.
Oh, I., Kim, M. & Kim, J. (2015). *Energy*, **86**, 292–299.
O'Regan, B. & Grätzel, M. (1991). *Nature*, **353**, 737–740.
Reis, K. P., Ramanan, A. & Whittingham, M. S. (1992). *J. Solid State Chem.* **96**, 31–47.
Rodriguez-Carvajal, J. (1993). *Physica B*, **192**, 55–69.
Sanchez, C., Julián, B., Belleville, P. & Popall, M. (2005). *J. Mater. Chem.* **15**, 3559–3592.
Shukla, S., Chaudhary, S., Umar, A., Chaudhary, G. R. & Mehta, S. K. (2014). *Sens. Actuators B Chem.* **196**, 231–237.
Song, Z., Wang, L. & Zhao, T. (2001). *Anal. Lett.* **34**, 399–413.
Stephens, J. S. & Cruickshank, D. W. J. (1970). *Acta Cryst.* B**26**, 222–226.
Szilágyi, I. M., Madarász, J., Pokol, G., Király, P., Tárkányi, G., Saukko, S., Mizsei, J., Tóth, A. L., Szabó, A. & Varga-Josepovits, K. (2008). *Chem. Mater.* **20**, 4116–4125.
Tilley, R. J. D. (1995). *The Crystal Chemistry of the Higher Tungsten Oxides*. In *The Chemistry of Non-Sag Tungsten*, pp. 93–109. Elsevier.
Umar, S., Rahman, M. M. & Hahn, Y. B. (2009). *Talanta*, **77**, 1376–1380.
Vogel, A. & Svehla, G. (1979). *Vogel's Textbook of Macro and Semimicro Qualitative Inorganic Analysis*, 5th ed. London: Longman.
Wang, G., Gu, A., Wang, W., Wei, Y., Wu, J., Wang, G., Zhang, X. & Fang, B. (2009). *Electrochem. Commun.* **11**, 631–634.
Wang, J., Toby, B. H., Lee, P. L., Ribaud, L., Antao, S., Kurtz, C., Ramanathan, M., Von Dreele, R. B. & Beno, M. A. (2008). *Rev. Sci. Instrum.* **79**, 085105.
Wasserman, H. H. & Vinick, F. J. (1973). *J. Org. Chem.* **38**, 2407–2408.
Werner, P.-E., Eriksson, L. & Westdahl, M. (1985). *J. Appl. Cryst.* **18**, 367–370.
Yamaguchi, A., Ichishima, I., Shimanouchi, T. & Mizushima, S. (1959). *J. Chem. Phys.* **31**, 843.
Yin, W. X., Li, Z. P., Zhu, J. K. & Qin, H. Y. (2008). *J. Power Sources*, **182**, 520–523.
Zare, H. R. & Habibirad, A. M. (2006). *J. Solid State Electrochem.* **10**, 348–359.
Zhou, T., Lu, P., Zhang, Z., Wang, Q. & Umar, A. (2016). *Sens. Actuators B Chem.* **235**, 457–465.